Металлофиз. новейшие технол. / Metallofiz. Noveishie Tekhnol.
2013, т. 35, № 1, сс. 1–17
Оттиски доступны непосредственно от издателя
Фотокопирование разрешено только
в соответствии с лицензией

ЭЛЕКТРОННЫЕ СТРУКТУРА И СВОЙСТВА

PACS numbers: 71.15.Rf, 71.20.Nr, 71.55.Gs, 75.30.Et, 75.50.Pp, 78.20.Ls, 78.70.Dm

Electronic Structure and X-Ray Magnetic Circular Dichroism in (Zn, T)O (T = V, Fe, Co) Diluted Magnetic Semiconductors

L. V. Bekenov, D. V. Mazur, V. N. Antonov, L. P. Germash*, and A. Ernst**

G. V. Kurdyumov Institute for Metal Physics N.A.S.U.,
36 Academician Vernadsky Blvd.,
UA-03680 Kyiv-142, Ukraine
**National Technical University of Ukraine*
'Kyiv Polytechnic Institute',
14 Politekhnichna Str.,
03056 Kyiv, Ukraine
***Max Planck Institute of Microstructure Physics,*
Weinberg, 2,
D-06120 Halle, Germany

The electronic structure of the (Zn, T)O (T = V, Fe, Co) diluted magnetic semiconductors is investigated theoretically from first principles, using the fully relativistic Dirac linear muffin-tin orbital band structure method. The X-ray absorption spectra, X-ray magnetic circular dichroism spectra at the Co, Fe, and V $L_{2,3}$ edges are investigated theoretically. The origin of the dichroism spectra in such compounds is examined. Using the magnetic force theorem, as it is implemented within the multiple scattering theory, the exchange interaction parameters for the transition metal atoms are calculated.

За допомогою зонної повністю релятивістської лінійної методи МТ-орбіталей теоретично досліджено з перших принципів електронні структури розбавлених магнетних напівпровідників (Zn, T)O (T = V, Fe, Co). Теоретично досліджено спектри поглинання Рентґенового випромінення і спектри Рентґенового магнетного циркулярного дихроїзму на $L_{2,3}$-краях поглинання атомів Co, Fe та V. Вивчено природу спектрів дихроїзму в цих сполуках. За допомогою теореми про магнетні сили на основі теорії багатократного розсіяння було обчислено параметри обмінної взаємодії між атомами перехідних металів.

Электронная структура разбавленных магнитных полупроводников (Zn, T)O (T = V, Fe, Co) исследована теоретически, исходя из первых принципов, полностью релятивистским линейным методом МТ-орбиталей. Теоретически исследованы рентгеновские спектры поглощения и спектры рентгеновского

циркулярного дихроизма на $L_{2,3}$-краях поглощения атомов Co, Fe и V. Изучена природа спектров дихроизма. С помощью теоремы о магнитных силах на основе теории многократного рассеяния вычислены параметры обменного взаимодействия между атомами переходных металлов.

Key words: diluted magnetic semiconductors, electronic structure, exchange interaction, magnetic properties, X-ray magnetic circular dichroism.

(Received August 28, 2012)

1. INTRODUCTION

Spintronics or spin-transport electronics has attracted much attention due to its technologically potential applications. Diluted magnetic semiconductors (DMSs) obtained by doping the host semiconductor with magnetic element impurities can be used for spintronics devices [1]. The starting materials, which were expected to be the promising candidates for spintronics, are Group III–V materials, such as (Ga, Mn)As with the highest Curie temperature of 110 K [2]. Other candidates are transition metal doped Group III nitrides, phosphides and semiconducting oxides. Dietl *et al.* [3] predicted theoretically that transition element doped semiconducting materials such as GaN and ZnO have a Curie temperature T_C higher than room temperature. After the report of $T_C = 280$ K in $(Zn_{1-x}Co_x)O$ [4], there have been many reports on ZnO-based DMSs showing high T_C [5].

As a wide-band-gap Group II–VI semiconductor, ZnO has recently been considered as a base material for transparent DMSs. Since ZnO has an energy band gap in the ultraviolet region (3.3 eV) and a large exciton binding energy (60 meV at room temperature) and can be made highly conductive by appropriate doping, it has attracted considerable attention as a material for optoelectronic device applications. Recently, it has been reported that V doping can cause ferromagnetism (FM) in ZnO. However, not much work has been done on the system and the results obtained so far are rather controversial. There have been a number of reports on the growth of $(Zn_{1-x}Co_x)O$ films [4, 6, 7] and characterization of their structural, magnetic and optical properties. However, substantial disagreement as to the magnetic and optical properties of magnetic alloys has been found. Despite the partial success, the nature of the host-impurity couplings, and of the ferromagnetic interactions in transition metal doped oxides, is not very well understood. The accumulated experience of experiments with thin films of magnetically doped semiconductors indicates a high sensitivity of the samples to the technology of their preparation and subsequent heat treatment [8].

The interest of previous investigations was to a great extent concentrated on the nature of the magnetic interactions in the DMSs. In the

present study, we focus our attention on X-ray absorption spectra (XAS) as well as X-ray magnetic circular dichroism (XMCD) in the (Zn, T)O (T = V, Fe, Co) DMSs. The XMCD experiments measure the difference of the absorption of X-rays with opposite (left and right) directions of circular polarization. The XMCD is a powerful tool to study the element-specific local magnetic interactions, and it reflects the spin and orbital polarizations of the local electronic states. The XAS and XMCD in the Co-doped ZnO were measured by several groups [9–26]. Field and temperature dependences of the XAS and XMCD spectra at the V $L_{2,3}$ edges in the (Zn, V)O were reported by Ishida *et al.* [27]. They found a linear increase of the XMCD signal with external magnetic field **H**, which indicates that the paramagnetic signal dominates the XMCD signal and that the ferromagnetic component is small, consistent with their magnetization measurements. The XAS and XMCD at the Fe $L_{2,3}$ edges in the Fe-doped ZnO were measured by several groups [28–31] as well.

2. COMPUTATIONAL DETAILS

The calculations of the electronic structure of (Zn, T)O (T = V, Fe, Co) DMSs were performed for a $3a\times3a\times1c$ and $3a\times3a\times2c$ supercells of the wurtzite-type ZnO unit cell with one or two of the Zn ions replaced by T. The supercell calculations were performed for the compositions $x = 0.0556$ (1/18) and $x = 0.02778$ (1/36) using the simple trigonal $P3m1$ (No. 156) space group. The substitutional $(Zn_{1-x}Co_x)O$ positions are illustrated in Fig. 1 for 72-atom ZnO unit cell containing two substitutional Co atoms $x = 0.0556$ (2/36). The Co atom has four O nearest neighbours: three O atoms at the distance of 1.949 Å and one O atom at

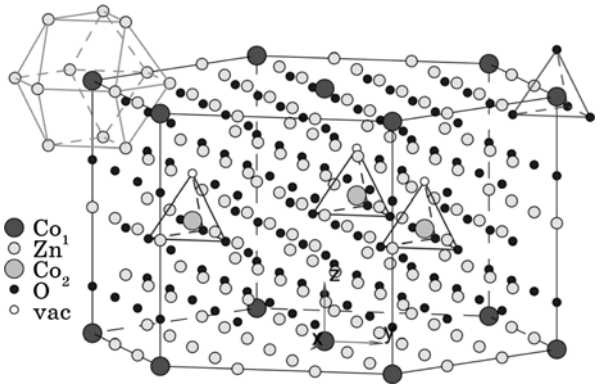

Fig. 1. Schematic representation of the $3a\times3a\times2c$ supercell of the wurtzite-type ZnO unit cell with two of the Zn ions replaced by Co ones. Small open circles show the oxygen vacancy in close vicinity of the Co_2 atom.

1.950 Å. The second-neighbour shell consists of 12 Zn atoms: six at the distance of 3.196 Å and six at 3.172 Å.

The details of the computational method are described in our previous papers [32–34], and here we only mention some aspects specific to the present calculations. The calculations presented in this work were performed using the spin-polarized relativistic linear-muffin-tin-orbital (SPR LMTO) method [35, 36] for the experimentally observed lattice constants $a = 9.588$ Å, $c = 5.16$ Å for wurtzite-type ZnO [37]. The crystal structure was optimized using the Vienna *ab initio* simulation package (VASP) [38–40]. For the LMTO calculations, we used the Perdew–Wang [41] parameterization of the exchange-correlation potential. Brillouin zone (BZ) integrations were performed using the improved tetrahedron method [42] and charge self-consistency was obtained on a grid of 95 **k** points in the irreducible part of the BZ. To improve the potential, we included additional interstitial spheres. The basis consisted of Co and Zn *s*, *p*, *d* and *f*, O *s*, *p* and *d*, and empty spheres *s* and *p* LMTOs.

3. RESULTS AND DISCUSSION

3.1. (Zn, Co)O and (Zn, Fe)O DMSs

3.1.1. Energy Band Structure

Figure 2 presents total and partial density of states for 72-atom ZnO wurtzite unit cell containing one CoZn substitution ($x = 0.03$) in the local spin density approximation (LSDA) and a ferromagnetic arrangement of the Co moments. The O 2*s* states are located mostly between –19.7 to –18.7 eV below the Fermi level (not shown) and the *p* states of O are found between –8.7 eV to –1.8 eV. The spin splitting of the O *p* states is quite small. Zn *d* states occupy the energy interval between –8.8 and –1.8 eV and hybridize strongly with the O 2*p* states. The Co 3*d* impurity states hybridize well with the O 2*p* conduction band, which gives a metallic character solution. The crystal field at the CoZn site (C_{3v} point symmetry) causes the splitting of Co *d* orbitals into a singlet a_1 (d_{3z^2-1}) and two doublets *e* (d_{yz} and d_{xz}) and e_1 (d_{xy} and $d_{x^2-y^2}$). In close vicinity to the Fermi level, a very strong narrow two-peak structure of the minority-spin Co d_{xz} and $d_{x^2-y^2}$ states is found (see the insert in the bottom panel of Fig. 2). The energy splitting between the two peaks is around 14 meV. The Fermi level is situated at the shoulder of the second high-energy peak. Peaks of d_{xz} and $d_{x^2-y^2}$ symmetry occur in the minority-spin channel at 0.45 to 0.67 eV above the Fermi level. The energy interval from 0.6 to 0.7 eV above the

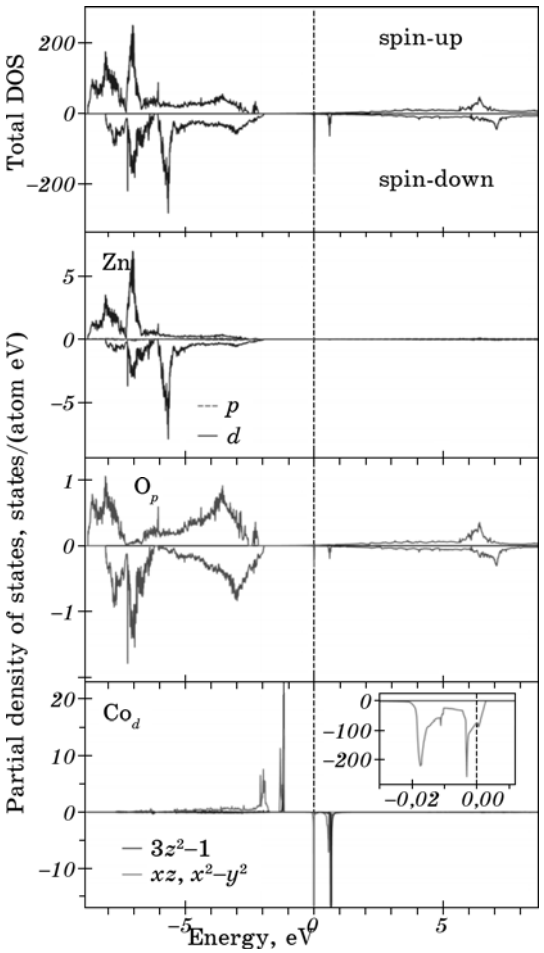

Fig. 2. The LSDA total [in states/(cell eV)] and partial [in states/(atom eV)] densities of states for the O, Zn and substitutional Co ions in $(Zn_{1-x}Co_x)O$ ($x = 0.03$) [43]. The insert is a blow-up of the Co d partial density of states close to the Fermi energy. The Fermi energy is at zero.

Fermi level is occupied by d_{3z^2-1} states with minority-spin.

The magnetic moment in the (Zn, Co)O unit cell is $3.947\mu_B$. Our band structure calculations yield the spin magnetic moment of $3.412\mu_B$ for the Co atoms in $(Zn_{1-x}Co_x)O$ ($x = 0.03$). The induced spin magnetic moments at the O first neighbour sites are of $0.048\mu_B$ and $0.173\mu_B$, for longer and shorter distant O atoms, respectively. Twelve Zn ions in the second neighbour shell couple ferromagnetically to the substitutional Co ion with spin magnetic moments from $0.014\mu_B$ to $0.043\mu_B$. The orbital moments at the Zn and O sites are small with the largest one at the O

first neighbour sites ($-0.011\mu_B$). The orbital magnetic moment at the Co site is $0.353\mu_B$ and is parallel to the spin moment. It is well known that the physical properties of ZnO are very sensitive to different kinds of defects in the crystal. In spite of numerous experimental studies, there is still controversy as to what the relevant native defects of this oxide are. Single-crystal ZnO has always been observed to contain Zn excess or oxygen deficiency [44]. The Zn excess can be accommodated in part by the presence of zinc interstitials or oxygen vacancies. Experiments have been inconclusive as to which of these is the predominant defect. Results presented in the literature point toward both possibilities and different interpretations have even been taken on the same set of experimental data (see, *e.g.*, [45]). However, several authors pointed out that oxygen vacancies were the predominant defect. Their conclusions were based on calculation of reaction rates [45], diffusion experiments [46] as well as electrical conductivity and Hall effect measurements [47]. To investigate the influence of possible oxygen vacancies on the electronic structure of the $(Zn_{1-x}Co_x)O$ DMSs, we perform the LMTO band structure calculations with two of the Zn ions replaced by Co with different environments. The supercell calculations were performed for the composition $x = 0.0625$ (2/36). We create an oxygen vacancy in the first neighbourhood of the second cobalt along z direction. The oxygen vacancy has four nearest neighbour atoms: three Zn atoms at the distance of 1.9496 Å and one Co atom at 1.9505 Å. The lattice relaxation was found to be very important in the presence of the oxygen vacancy. The lattice relaxation causes the shift of the Co_2 atom and the three Zn atoms toward the vacant site by 0.13 Å and 0.24 Å, respectively.

3.1.2. X-Ray Absorption and XMCD Spectra at the Co $L_{2,3}$ Edges

Figure 3 presents experimental XAS and XMCD spectra [25] of (Zn, Co)O at the Co $L_{2,3}$ edges together with the spectra calculated in the LSDA. The X-ray absorption spectrum at the Co L_3 edge is rather complicated and consists of two major structures: peak b at around 780.9 eV with a low energy shoulder a at 780 eV and double peak c at 781.6–782.4 eV with high energy fine structure d at 784 eV. As may be seen from the top panel of Fig. 3, the calculations for the ideal crystal structure with one substitutional Co_1 atom (full curve) provide the X-ray absorption intensity only at the peaks a and b. The full explanation of the spectra is only possible by taking crystal imperfections, such as oxygen deficiency, into account. The oxygen vacancy (with lattice relaxation taken into account) strongly affects the shape of the XAS spectra. As may be seen from Fig. 3 (top panel), the X-ray absorption from the Co_2 atoms with the oxygen vacancy (dashed line) mostly determines the shape of the major double peak c. Thereby, our calculations including oxygen deficiency reproduce the shape of the Co L_3 X-

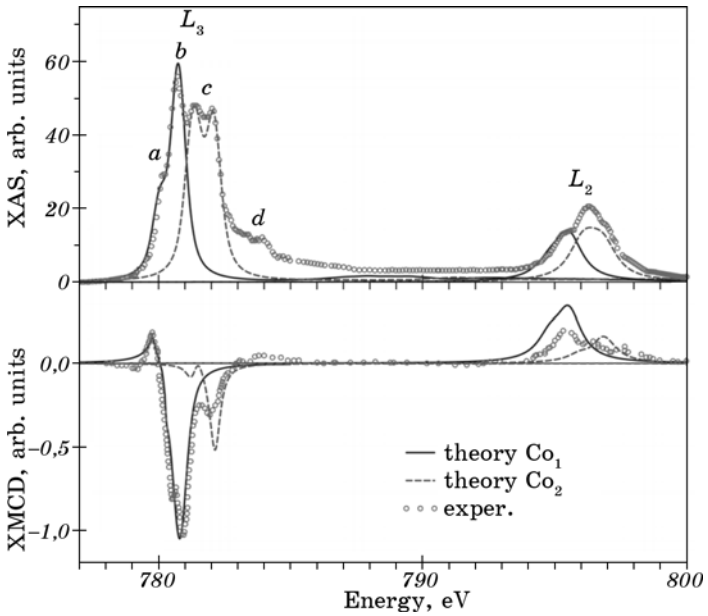

Fig. 3. X-ray absorption (top panel) and XMCD (lower panel) experimental spectra [25] (circles) of $(Zn_{1-x}Co_x)O$ ($x = 0.07$) at the Co $L_{2,3}$ edges and theoretically calculated spectra [43] for the Co_1 without any additional defects (full lines) and Co_2 with the oxygen vacancy (dashed lines) ions. The experimental spectra were measured at $H = 7$ T and $T = 20$ K [25].

ray absorption spectrum quite well except for the high energy structure *d*. It might be that the additional satellite structure at the high-energy tail of the Co L_3 XAS appears due to many-body effects. This question needs an additional theoretical investigation using an appropriate many-body treatment. The theoretically calculated Co $L_{2,3}$ XMCD spectra are in good agreement with the experiment (lower panel in Fig. 3). The high-energy minimum at around 782 eV was found to be due to the oxygen vacancy in the (Zn, Co)O DMS.

3.1.3. X-Ray Absorption and XMCD Spectra at the Fe $L_{2,3}$ Edges

The XAS and XMCD spectra at the Fe $L_{2,3}$ edges in Fe doped ZnO were measured by several groups [28–31]. Figure 4 presents experimental XAS and XMCD spectra [29] of (Zn, Fe)O at the Fe $L_{2,3}$ edges together with the calculated ones. The line shape of the XAS spectrum at the Fe L_3 edge in the (Zn, Fe)O DMS shows a two-peak structure with a major peak at 710 eV and a smaller one at 708.5 eV. The major peak possesses an additional high-energy shoulder. As may be seen from the top panel of Fig. 4, the calculations for the ideal crystal structure with one sub-

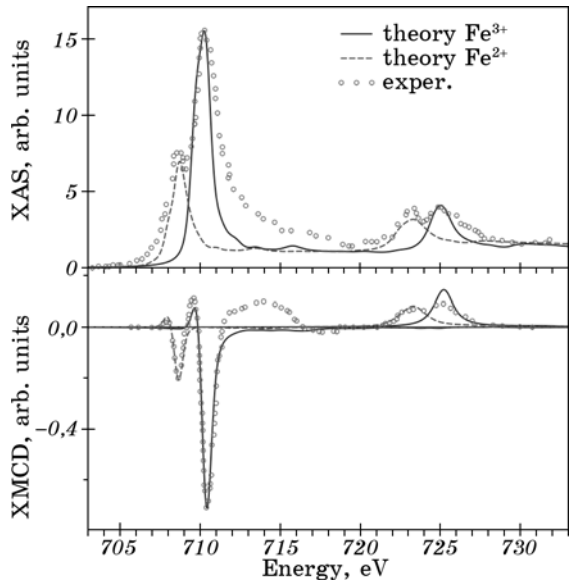

Fig. 4. X-ray absorption (top panel) and XMCD (lower panel) experimental spectra [29] (circles) of $(Zn_{1-x}Fe_x)O$ at the Fe $L_{2,3}$ edges and theoretically calculated spectra for the Fe_1^{3+} without any additional defects (full lines) and Fe_1^{2+} with the oxygen vacancy (dashed lines) ions.

stitutional Fe_1^{3+} ion (full curve) provide the X-ray absorption intensity at the major peaks only. The oxygen vacancy strongly affects the shape of the XAS spectra. As may be seen from Fig. 4 (top panel), the X-ray absorption from the Fe_2^{2+} atoms with the oxygen vacancy (dashed line) mostly determines the shape of the low energy peak at 708.5 eV. Thereby, our calculations including oxygen deficiency reproduce the shape of the Fe L_3 X-ray absorption spectrum quite well except for high-energy structure at 711–714 eV. It might be that the additional satellite structure at the high-energy tail of the Fe L_3 XAS appears due to many-body effects. The theoretically calculated Fe $L_{2,3}$ XMCD spectra are in good agreement with the experiment (lower panel in Fig. 4). The low energy minimum at around 708.5 eV was found to be due to the oxygen vacancy in the (Zn, Fe)O DMS. The theory does not produce the fine structure corresponding to the high-energy satellite structure at around 711–714 eV.

3.2. (Zn, V)O DMS

3.2.1. Electronic Structure

Figure 5 presents LSDA total and partial density of states for the ZnO

wurtzite unit cell containing one V substitution. The O *s* states are located mostly between –21.0 and –19.7 eV and the O *p* states are found between –9.6 eV and –3.0 eV. The spin splitting of the O *p* states is quite small. Zn *d* states occupy the energy interval between –9.6 eV and –3.0 eV and hybridize strongly with the O *p* states. The majority-spin V d_{3z^2-1} structure is found in close vicinity to the Fermi energy between –0.2 eV and 0.7 eV (see the insert in the bottom panel of Fig. 5).

Very strong and narrow peaks of the majority-spin V bonding d_{xy} and d_{yz} states are located between –0.4 eV and –0.8 eV. The corresponding

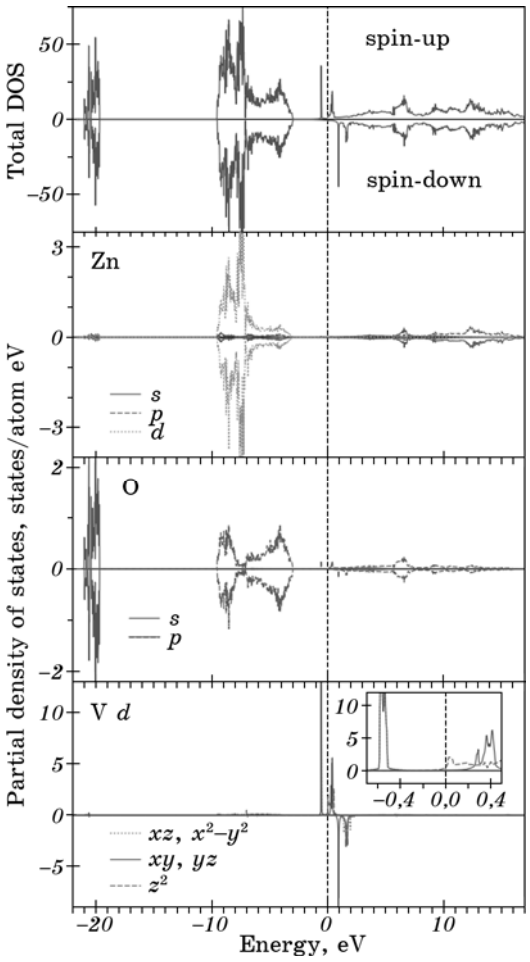

Fig. 5. The LSDA total [in states/(cell eV)] and partial [in states/(atom eV)] densities of states for the O, Zn and substitutional V ions in $(Zn_{1-x}V_x)O$ ($x = 0.06$) [48]. The insert is a blow-up of the V *d* partial density of states close to the Fermi energy. The Fermi energy is at zero.

anti-bonding states are from 0.2 eV to 0.6 eV. Narrow peaks of d_{xy} and d_{yz} symmetry occur in the minority-spin channel at around 1 eV above the Fermi level. The energy interval from 1.4 eV to 2.2 eV above the Fermi level is occupied by the d_{xz}, $d_{3x^2-y^2}$ and d_{3z^2-1} minority-spin states.

We also investigated the electronic and magnetic structures of the $(Zn_{1-x}V_x)O$ DMSs with two of Zn ions replaced by V. The supercell calculations were performed for the compositions $x = 0.1111$ (2/18), $x = 0.0625$ (2/32) and $x = 0.0555$ (2/36). We found that vanadium atoms placed at different Zn sites show very little selectivity of site occupancy. Besides, different geometries with ferromagnetic and antiferromagnetic (AFM) configurations are found to be energetically nearly degenerate, the difference in the total energies between ferromagnetic and antiferromagnetic solutions was found to be less than 3 meV per a formula unit. Still in most cases, the ferromagnetic solutions are lower in total energy in comparison with the antiferromagnetic solutions. However, for fully relaxed lattice we found that the AFM ordering has lower total energy in comparison with the FM one.

3.2.2. XAS and XMCD Spectra

The X-ray absorption and X-ray magnetic circular dichroism of the dilute magnetic semiconductor (Zn, V)O at the V $L_{2,3}$ edges have been investigated by Ishida *et al.* [27]. They found that 90% of the V ions were presumably strongly antiferromagnetically coupled, and the ferromagnetic component was below the detection limit of XMCD.

Since the real structure and chemical composition of $(Zn_{1-x}V_x)O$ was not known, we performed numerous calculations fitting XAS and XMCD spectra to the experimental results. The fitting parameters were positions of V atoms, Zn excess atoms, various oxygen vacancies and the magnetic order of V atoms. The best fit is shown in Fig. 6, which presents the calculated XAS as well as XMCD spectra of the $(Zn_{1-x}V_x)O$ DMS at the V $L_{2,3}$ edges compared with the experimental data [27]. In this model, V atoms substitute cations and are antiferromagnetically ordered. Also, they are positioned at the largest possible V_1–V_2 distance of 5.53 Å. Relevant XMCD signal occurs only in the presence of an oxygen vacancy located in the first neighbourhood of the second V_2 atom along z direction. Adding Zn excess atoms also improves the agreement between theory and experiment. The X-ray absorption spectrum at the V L_3 edge is rather complicated and consists of two major peaks c and d at 515.6 eV and 517 eV, respectively, with two additional low energy shoulders a and b at 513.8 eV and 514.6 eV and a high energy shoulder at 518 eV. As can be seen from the top panel of Fig. 6, the calculations for the ideal crystal structure with two substitutional AFM ordered V_1 atoms (full curve) provide the X-ray absorption intensity only at the peak c and the shoulder b. The full expla-

nation of the spectra is only possible by considering crystal imperfections. We investigate the influence of two types of crystal defects on the XAS and XMCD spectra, namely, oxygen deficiency and Zn excess. The oxygen vacancy strongly affects the shape of the XAS spectra.

As can be seen from Fig. 6 (top panel), the X-ray absorption from the V_2 atoms with the oxygen vacancy (dashed line) contributes to the major peak *c* and significantly determines the intensity of the peak *d* and the high energy shoulder *e*. To investigate the Zn excess on the XMCD spectra, we placed an extra Zn atom into the tetrahedral interstitial position, which is 2.1916 Å apart from the V_2 site. The X-ray absorption from the V_{Zn} atoms with the Zn excess atom (dotted line) contributes to the major peaks *c* and *d* as well as to both the low energy shoulders *a* and *b*. Thereby, our simulation including oxygen deficiency and

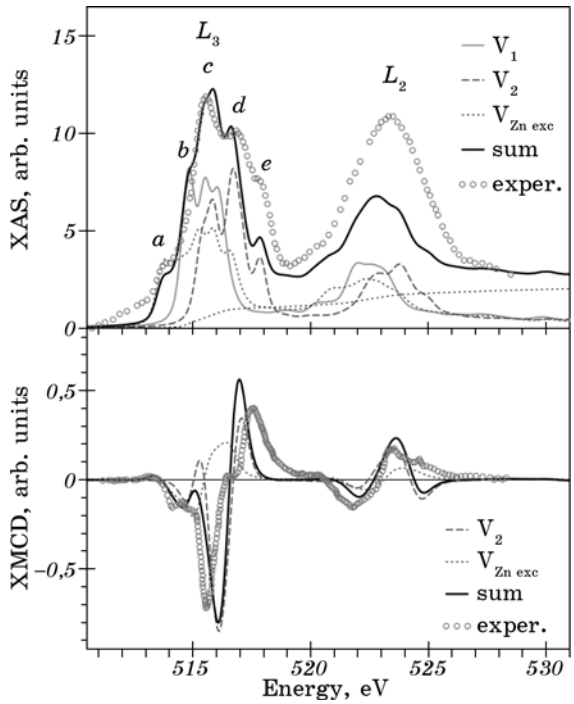

Fig. 6. Top panel: theoretically calculated (thick full line) [48] and experimentally measured [27] (circles) X-ray absorption spectra of $(Zn_{1-x}V_x)O$ at the V $L_{2,3}$ edges. Full line presents the X-ray absorption spectrum without any additional defects. Dashed and dotted lines present the XA spectra with the oxygen vacancy (the contribution of the V_2 sublattice as in Fig. 1) and Zn excess atom, respectively. Bottom panel: theoretically calculated (thick full line) and experimentally measured [27] (circles) XMCD spectra at the V $L_{2,3}$ edges. Dashed and dotted lines present the XMCD spectra with the oxygen vacancy and Zn excess atom, respectively.

Zn excess reproduces the shape of the V L_3 X-ray absorption spectrum quite well (see thick curve in top panel of Fig. 6). The lattice relaxation was found to be very important in the presence of the oxygen vacancy as well as the Zn excess.

The XMCD spectrum at the V L_3 edge is also rather complicated and consists of a small positive peak at 513.8 eV, a negative fine structure at 514.6 eV, a negative major peak at 515.6 eV, and a positive major peak at 517.7 eV with a shoulder at 516.4 eV. The V L_2 XMCD spectrum consists of two major fine structures, a negative peak at 521.8 eV and a positive one at 523.3 eV. The theory is not able to reproduce the shape and relative intensity of the V $L_{2,3}$ XMCD spectra for the ferromagnetically ordered V atoms, with one and two V substitutions per unit cell. The theory strongly overestimates (from one to two orders of magnitude) the dichroism signal and produces non-adequate shape of the spectra. On the other hand, the theory produces an almost vanishing XMCD signal for the AFM ordering of vanadium substitutional V ions for the ideal crystal structure without any kind of defects due to cancellation of the XMCD spectra with opposite spin directions. We should mention that any shift from the antiferro- to the ferrimagnetic ordering will increase the intensity of the final XMCD spectra due to the reduction of the compensation of the XMCD spectra from V ions with opposite spin directions. Such a shift may be caused by an applied external magnetic field or different kinds of defects and imperfections in the lattice. The experimental measurements were performed in an external magnetic field of 7 T [27]. We have performed the calculations with an external magnetic field applied along z direction and, indeed, obtained the spectra increase, but only by approximately 10 to 20%. We found that only the defects cause a significant difference. As can be seen from the lower panel of Fig. 6, the theoretically calculated XMCD spectra with an oxygen vacancy (dashed line) resemble the experimental spectra quite well. An additional consideration of the Zn excess atoms (dotted curve) leads to further improvement between the theory and the experiment. One should mention that we obtain better agreement between the theory and the experiment in the X-ray absorption rather than in the XMCD spectra. The energy splitting between the two major peaks of the V L_3 XMCD spectrum was found to be smaller than the experimentally measured one. The reproduction of the shape of the V $L_{2,3}$ XMCD spectra is a quite difficult task because the rather weak final XMCD signal is derived from two large signals occurring from the V atoms with opposite spin directions. In this case, we have to take into account different crystal defects in a particular sample with quite precise relative concentration. However, the type and concentration of possible defects in a sample is not always well known. On the other hand, the extreme sensitivity of the XMCD signal may be considered as a useful tool to reveal the details of the composition by modelling numerically different types of defects and

comparing the theoretically calculated XMCD spectra with the experimentally measured ones.

3.2.3. Exchange Interactions

To describe the magnetic properties of $(Zn_{1-x}V_x)O$, we calculated exchange interactions between magnetic moments using the magnetic force theorem as it is implemented within the multiple scattering theory [49]. The structural model, elucidated from our XAS and XMCD simulations, was utilized for calculations of the corresponding electronic structure and exchange parameters using the KKR Green function method in the multiple scattering representation [50]. The schematic representation of the exchange interaction between the magnetic moments of the nearest neighbours is shown in Fig. 7.

The strongest magnetic interactions were found between V atoms only if there is either an oxygen atom or an oxygen vacancy in between (see Fig. 7, *a* and 7, *b*, respectively). Thereby, one can distinguish two different vanadium atoms: V_1 far from and V_2 close to an oxygen vacancy. The exchange interaction between V_1 and V_2 atoms is very small since the atoms are separated by 5.53 Å and there is no connecting atom in between. The V_1–V_1 exchange interaction is mediated mainly by the oxygen between the vanadium atoms and is positive leading to a ferromagnetic order in this pair (see J_{01}^{11} at zero relaxation in Fig. 8, *b*).

This behaviour changes by replacing the oxygen by a vacancy (V_2–V_2

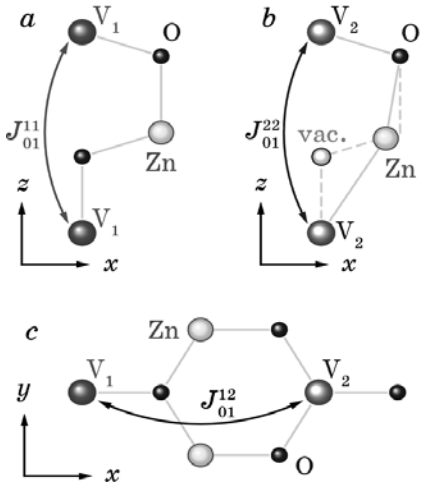

Fig. 7. Schematic representation of magnetic interactions between V atoms in $(Zn_{1-x}V_x)O$: two V atoms substituting Zn positions with an oxygen in between (*a*); two V atoms within an oxygen vacancy in between (*b*); V_1–V_2 pair (see the text for explanation) (*c*). The dashed line in (*b*) shows ideal wurtzite structure.

pair) in accordance to our structural model. Removing the oxygen atom kills the exchange interaction between the neighbouring vanadium moments (see J_{01}^{22} at zero relaxation in Fig. 8, *b*). However, the atoms around the vacancy experience strong relaxations and this promotes an antiferromagnetic order in this pair. Our simulations show that the exchange interaction is very sensitive to these atomic movements.

We found that the most substantial changes of J_{ij} occur when the neighbouring Zn atoms move towards the vacancy (see inset in Fig. 8), while relaxations of V and O atoms are insignificant for the magnetic interaction. According to our structural optimizations, the shift of the Zn atoms is about 0.26 Å. Due to these relaxations, the exchange parameters for the first neighbours J_{01}^{22} were changed from 0 meV in the non-relaxed geometry to −16 meV. The exchange interaction between the second neighbours also experiences significant changes, and, in the relaxed geometry, it is positive. This suggests that the V_2–V_2 pair with an oxygen vacancy is antiferromagnetic. The vanadium pairs V_1–V_1 without oxygen vacancies remain ferromagnetic, although the value of the exchange parameters J_{01}^{11} reduces from 5.8 meV in the non-relaxed case to 2.6 meV after relaxation. The critical temperature, estimated within the random

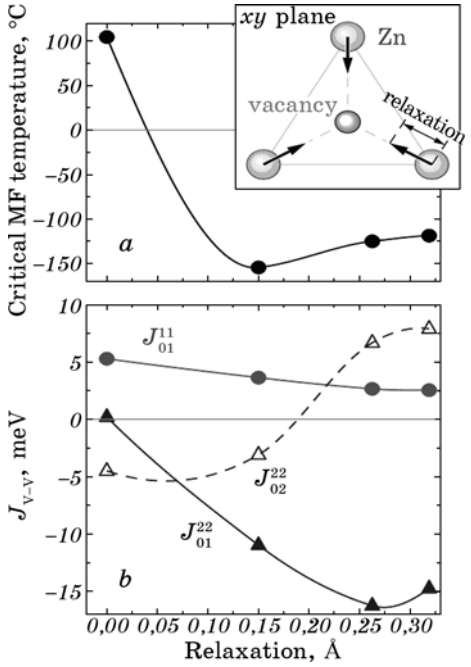

Fig. 8. Critical temperatures (*a*) and exchange parameters (*b*) for $(Zn_{1-x}V_x)O$ calculated for various positions of atoms around an oxygen vacancy [48]. Inset shows scheme of movements of Zn atoms towards the vacancy.

phase approximation, is about 120 K in the relaxed geometry.

The most important question is why the relaxations of Zn atoms around the vacancy lead to such substantial changes of magnetic interactions. The Zn states are deep in the valence bands and do not hybridize with the V states, which are located close to the Fermi level (see Fig. 5). Relaxations of oxygen atoms were found to be very small and do not change magnetic properties of $(Zn_{1-x}V_x)O$. However, the hybridization between V 3*d* and oxygen 2*p* states is strongly affected by the relaxations of the Zn atoms, which is evidently crucial for the magnetic interactions in this system. Our analysis of the density of states and occupation numbers yields a significant increase of the hybridization between V 3*d* and O 2*p* states. This is governed by stronger *d*–*d* hybridization between Zn atoms moved towards the vacancy and, at the same time, due to decreasing the hybridization between these Zn 3*d* and O 2*p* states.

4. SUMMARY

The theory reproduces the shape and energy positions of major fine structures of the Co and Fe XAS and XMCD spectra at the $L_{2,3}$ edges in (Zn, Co)O and (Zn, Fe)O DMSs reasonably well. We show that oxygen deficiency is responsible for some fine structures of the Co and Fe L_3 XAS and XMCD spectra.

The shape of the V $L_{2,3}$ XMCD spectra might be explained only by suggesting the AFM ordering between the V ions situated at the largest possible $V^{\uparrow}$–$V^{\downarrow}$ distance from each other. The XMCD signal appears as superposition of very intensive dichroic signals from V ions with opposite spin directions. The relevant XMCD signal is obtained only in the presence of an oxygen vacancy located in the first neighbourhood of the second V atom. Adding extra Zn atoms improves the agreement between the theory and the experiment. The lattice relaxation was found to be very important in the presence of the oxygen vacancy as well as Zn excess.

The structure obtained from the comparison of the XMCD spectra and theoretical simulations was used to study magnetic properties of (Zn, V)O DMSs. Using the magnetic force theorem, as it is implemented within the multiple scattering theory, we have calculated the exchange interaction parameters for the V atoms. We have found that magnetic V ions form two magnetic pairs, one ferromagnetic and another antiferromagnetic, which interact weakly with each other. The antiferromagnetic order in one of the pairs is due to the presence of an oxygen vacancy and strongly relaxed positions of neighbouring Zn atoms.

ACKNOWLEDGMENTS

This work was supported by the National Academy of Sciences of

Ukraine in the framework of the State Target Scientific and Technology Program of Implementation and Application of Grid Technologies for 2009–2013.

REFERENCES

1. J. K. Furdyna, *Appl. Phys. Lett.*, **64**: R29 (1988).
2. H. Ohno, A. Shen, F. Matsukura et al., *Appl. Phys. Lett.*, **69**: 363 (1996).
3. T. Dietl, H. Ohno, F. Matsukura et al., *Science*, **287**: 1019 (2000).
4. K. Ueda, H. Tabata, and T. Kawai, *Appl. Phys. Lett.*, **79**: 988 (2001).
5. C. Liu, F. Yun, and H. Morko, *J. Mater. Sci.: Mater. Electronics*, **16**: 555 (2005).
6. K. Ando, H. Saito, Z. Jin et al., *Appl. Phys. Lett.*, **78**: 2700 (2001).
7. Y. Z. Yoo, T. Fukumura, Z. Jin et al., *J. Appl. Phys.*, **90**: 4246 (2001).
8. K. Kikoin, *Low Temp. Phys.*, **35**: 58 (2009).
9. M. Kobayashi, Y. Ishida, J. Hwang et al., *Phys. Rev. B*, **72**: 201201 (2005).
10. M. Gacic, G. Jakob, C. Herbort et al., *Phys. Rev. B*, **75**: 205206 (2007).
11. S. D. Brown, P. Strange, L. Bouchenoire et al., *Phys. Rev. Lett.*, **99**: 247401 (2007).
12. A. Ney, K. Ollefs, S. Ye et al., *Phys. Rev. Lett.*, **100**: 157201 (2008).
13. K. Rode, R. Mattana, A. Anane et al., *Appl. Phys. Lett.*, **92**: 012509 (2008).
14. M. Opel, K.-W. Nielsen, S. Bauer et al., *Eur. Phys. J. B*, **63**: 437 (2008).
15. T. Tietze, M. Gacic, G. Schutz et al., *New J. Phys.*, **10**: 055009 (2008).
16. N. R. S. Farley, K. W. Edmonds, A. A. Freeman et al., *New J. Phys.*, **10**: 055012 (2008).
17. T. Kammermeier, V. Neya, S. Yea et al., *J. Magn. Magn. Mater.*, **321**: 699 (2009).
18. A. P. Singh, R. Kumar, P. Thakur et al., *J. Phys.: Condens. Matter*, **21**: 185005 (2009).
19. S. Kumar, Y. J. Kim, B. H. Koo et al., *J. Korean Phys. Soc.*, **55**: 1060 (2009).
20. A. Ney, T. Kammermeier, K. Ollefs et al., *Phys. Rev. B*, **81**: 054420 (2010).
21. A. Ney, V. Ney, S. Ye et al., *Phys. Rev. B*, **82**: 041202 (2010).
22. V. Ney, S. Yea, T. Kammermeier et al., *J. Magn. Magn. Mater.*, **322**: 1232 (2010).
23. V. Ney, S. Ye, K. Ollefs et al., *J. Nanosci. Nanotechnol.*, **10**: 5958 (2010).
24. A. Ney, M. Opel, T. C. Kaspar et al., *New J. Phys.*, **12**: 013020 (2010).
25. M. Kobayashi, Y. Ishida, J. I. Hwang et al., *Phys. Rev. B*, **81**: 075204 (2010).
26. P. Photongkam, Y. B. Zhang, M. H. N. Assadi et al., *J. Appl. Phys.*, **107**: 033909 (2010).
27. Y. Ishida, J. I. Hwang, M. Kobayashi et al., *Appl. Phys. Lett.*, **90**: 022510 (2007).
28. T. Kataoka, M. Kobayashi, Y. Sakamoto et al., *J. Appl. Phys.*, **107**: 033718 (2010).
29. T. Kataoka, M. Kobayashi, G. S. Song et al., *Jpn. J. Appl. Phys.*, **48**: 04C200 (2009).
30. S. Gautam, S. Kumar, P. Thakur et al., *J. Phys. D: Appl. Phys.*, **42**: 175406 (2009).
31. T. Shinagawa, M. Izaki, K. Murase et al., *J. Electrochem. Soc.*, **153**: G168 (2006).
32. V. N. Antonov, H. A. Durr, Y. Kucherenko et al., *Phys. Rev. B*, **72**: 054441 (2005).
33. V. N. Antonov, O. Jepsen, A. N. Yaresko, and A. P. Shpak, *J. Appl. Phys.*, **100**: 043711 (2006).
34. V. N. Antonov, A. N. Yaresko, and O. Jepsen, *Phys. Rev. B*, **81**: 075209 (2010).
35. O. K. Andersen, *Phys. Rev. B*, **12**: 3060 (1975).

36. V. V. Nemoshkalenko, A. E. Krasovskii, V. N. Antonov et al., *phys. status solidi (b)*, **120**: 283 (1983).
37. S. Saib and N. Bouarissa, *Physica B*, **387**: 377 (2007).
38. P. E. Blochl, *Phys. Rev. B*, **50**: 17953 (1994).
39. J. P. Perdew, K. Burke, and M. Ernzerhof, *Phys. Rev. Lett.*, **78**: 1396 (1997).
40. G. Kresse and J. Joubert, *Phys. Rev. B*, **59**: 1758 (1999).
41. J. Perdew and Y. Wang, *Phys. Rev. B*, **45**: 13244 (1992).
42. P. E. Blochl, O. Jepsen, and O. K. Andersen, *Phys. Rev. B*, **49**: 16223 (1994).
43. V. N. Antonov, L. V. Bekenov, O. Jepsen et al., *J. Appl. Phys.*, **111**: 073702 (2012).
44. M. Sukkar and H. Tuller, *Advances in Ceramics* (Eds. M. F. Yan and A. H. Heuer) (Columbus, OH: American Ceramic Society: 1983), vol. **7**, p. 71.
45. G. D. Mahan, *J. Appl. Phys.*, **54**: 3825 (1983).
46. J. W. Hoffman and I. Lauder, *Trans. Faraday Soc.*, **66**: 2346 (1970).
47. E. Ziegler, A. Heinrich, H. Oppermann, and G. Stove, *phys. status solidi (a)*, **66**: 635 (1981).
48. L. V. Bekenov, V. N. Antonov, S. Ostanin et al., *Phys. Rev. B*, **84**: 134421 (2011).
49. A. I. Liechtenstein, M. I. Katsnelson, V. P. Antropov, and V. A. Gubanov, *J. Magn. Magn. Mater.*, **67**: 65 (1987).
50. M. Luders, A. Ernst, W. M. Temmerman et al., *J. Phys.: Condens. Matter*, **13**: 8587 (2001).